Available online at www.sciencedirect.com
ScienceDirect
Quaternary Research 69 (2008) 130–144
QUATERNARY RESEARCH
www.elsevier.com/locate/yqres

Last glacial maximum climate inferences from cosmogenic dating and glacier modeling of the western Uinta ice field, Uinta Mountains, Utah

Kurt A. Refsnider [a,*], Benjamin J.C. Laabs [b], Mitchell A. Plummer [c], David M. Mickelson [a], Bradley S. Singer [a], Marc W. Caffee [d]

[a] *Department of Geology and Geophysics, University of Wisconsin, 1215 W Dayton St., Madison, WI 53706, USA*
[b] *Department of Geological Sciences, SUNY Geneseo, 1 College Circle, Geneseo, NY 14454, USA*
[c] *Idaho National Laboratory, Idaho Falls, ID 83415-2107, USA*
[d] *Department of Physics, Purdue University, 1296 Physics Building, W. Lafayette, IN 47907, USA*

Received 30 January 2007
Available online 4 January 2008

Abstract

During the last glacial maximum (LGM), the western Uinta Mountains of northeastern Utah were occupied by the Western Uinta Ice Field. Cosmogenic ^{10}Be surface-exposure ages from the terminal moraine in the North Fork Provo Valley and paired ^{26}Al and ^{10}Be ages from striated bedrock at Bald Mountain Pass set limits on the timing of the local LGM. Moraine boulder ages suggest that ice reached its maximum extent by 17.4±0.5 ka (±2σ). ^{10}Be and ^{26}Al measurements on striated bedrock from Bald Mountain Pass, situated near the former center of the ice field, yield a mean ^{26}Al/^{10}Be ratio of 5.7±0.8 and a mean exposure age of 14.0±0.5 ka, which places a minimum-limiting age on when the ice field melted completely. We also applied a mass/energy-balance and ice-flow model to investigate the LGM climate of the western Uinta Mountains. Results suggest that temperatures were likely 5 to 7°C cooler than present and precipitation was 2 to 3.5 times greater than modern, and the western-most glaciers in the range generally received more precipitation when expanding to their maximum extent than glaciers farther east. This scenario is consistent with the hypothesis that precipitation in the western Uintas was enhanced by pluvial Lake Bonneville during the last glaciation.

Keywords: Uinta Mountains; Last glacial maximum; Cosmogenic nuclide; CRN; Glacier modeling; Ice field; Lake Bonneville; Glacial geology; Paleoclimate

Introduction

Alpine glaciers are sensitive indicators of changes in climate (Oerlemans et al., 1998) and respond on sub-millennial timescales (Paterson, 1994). Thus, paleoclimatic inferences are commonly made based on the extent of past mountain glaciers. Throughout the western U.S., reconstructions of alpine paleoglaciers and associated equilibrium line altitudes (ELAs) have been used to determine possible precipitation and temperature combinations that supported glaciers during the last glacial maximum (LGM; e.g. Leonard, 1984, 1989; Munroe and Mickelson, 2002; Brugger, 2006). In order to put these glaciological reconstructions into a temporal context, a firm chronology of past glacial advances must be established. With the advent of cosmogenic nuclide surface-exposure dating, broad patterns in the timing of mountain glacier advances across the western U.S. and related patterns of regional and temporal variations in paleoclimate conditions are emerging (e.g., Gosse et al., 1995; Phillips et al., 1997; Licciardi et al., 2001, 2004; Owen et al., 2003; Benson et al., 2004, 2005; Brugger, 2006; Munroe et al., 2006). However, dated glacial features in most ranges of the Rocky Mountains are still scarce, and improving the knowledge of regional climate during the LGM requires a more comprehensive temporal record of glacial advances and retreat and accurate techniques for estimating paleoclimatic conditions based on the glacial record.

The Uinta Mountains of northeastern Utah (Figs. 1a and b) were extensively glaciated during the LGM (Atwood, 1909; Oviatt, 1994; Laabs and Carson, 2005; Munroe, 2005). The first

* Corresponding author. Current address: Institute of Arctic and Alpine Research, 1560 30th St. 450 UCB, Boulder, CO 80303, USA.
E-mail address: kurt.refsnider@colorado.edu (K.A. Refsnider).

0033-5894/$ - see front matter © 2007 University of Washington. All rights reserved.
doi:10.1016/j.yqres.2007.10.014

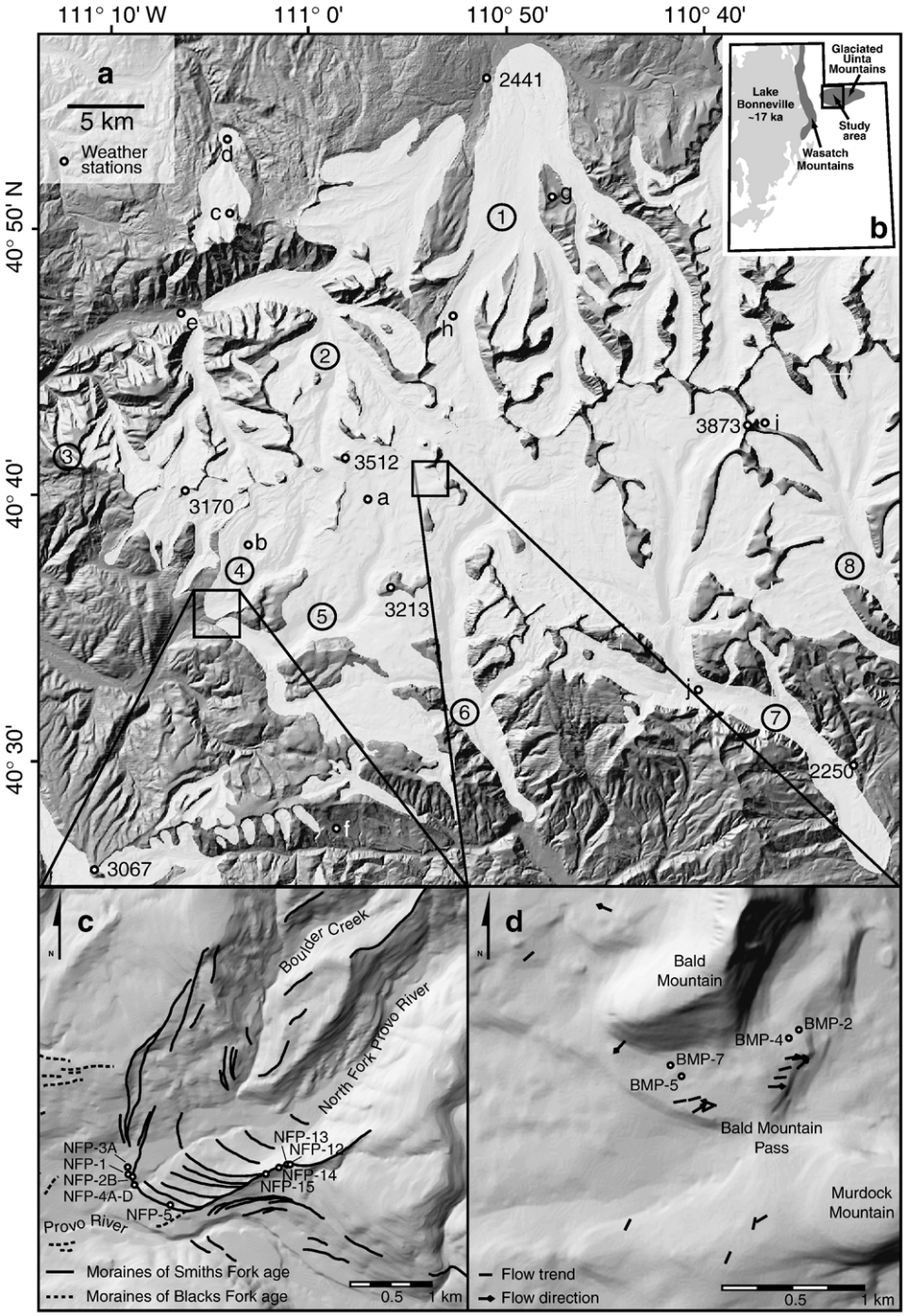

Figure 1. The western Uinta Mountains. (a) Shaded relief map of the study area with the ice extent during the LGM shown in white. Ice extents are based on mapping by Oviatt (1994), Munroe (2005), Laabs and Carson (2005), and Refsnider (2007). The extent of glaciers southwest of the Western Uinta Ice Field and a revised extent for ice in the Bear River drainage are also shown (Munroe, J.S., unpublished data). Drainages occupied by glaciers included in the modeling are indicated by circled numbers; 1: Bear River, 2: Main Weber; 3: Swifts Canyon, 4: North Fork Provo, 5: Main Fork Provo, 6: North Fork Duchesne, 7: Rock Creek, 8: Lake Fork. The Yellowstone drainage (study site of Laabs et al., 2006) is immediately east of the Lake Fork drainage (study site of Munroe et al., 2006; Laabs et al., 2006). The locations of weather stations are also included, though a few stations utilized for the modeling fall within the area covered by this map. Letters correspond to stations in Table 1. Uncircled numbers show point elevations in meters above sea level. (b) Utah and the relative locations of the glaciated Uinta Mountains, the Wasatch Range, and pluvial Lake Bonneville. (c) The locations of boulders sampled on the North Fork Provo terminal moraine for cosmogenic ^{10}Be surface-exposure dating. (d) The locations of striated bedrock surfaces at Bald Mountain Pass sampled for ^{10}Be and ^{26}Al surface-exposure dating.

cosmogenic ^{10}Be surface-exposure ages to constrain the timing of the *local* LGM (hereafter referred to simply as the LGM) in the Uinta Mountains suggest that glaciers near the southwestern end of the range remained at their maximum extent until 16.8± 0.7 ka, up to 3 ka later than glaciers in nearby ranges in Colorado and Wyoming (Munroe et al., 2006; note that the uncertainties in these cosmogenic ^{10}Be ages do not include the ca. 6% uncertainty in ^{10}Be production rate (Stone, 2000)). Pluvial Lake

https://doi.org/10.1016/j.yqres.2007.10.014 Published online by Cambridge University Press

Bonneville, which covered much of western Utah during the LGM and was ~50 km west of the western end of the Uinta Mountains (Fig. 1b), remained near its hydrologic maximum until ca. 17.5 cal ka BP (Oviatt, 1997; all radiocarbon ages calibrated using CALIB 5.0.2; Stuiver et al., 2005). Several previous studies have suggested that atmospheric circulation in the Great Basin region during the LGM was similar to modern, and that precipitation was enhanced due to a southward displacement of the polar jet and associated storm tracks (e.g., Benson and Thompson, 1987). McCoy and Williams (1985) suggested that lake effect snow derived from Lake Bonneville affected the mass balances of glaciers in the adjacent Wasatch and Uinta ranges, and Munroe and Mickelson (2002) and Munroe et al. (2006) noted that reconstructed LGM ELAs in drainages across the Uintas dropped ca. 600 m toward the western end of the range. This trend and the apparent synchroneity between the timing of the LGM in the southern part of the range and the regression of Lake Bonneville from its hydrologic maximum suggests that Lake Bonneville had considerable impact on the mass balances of glaciers in the Uinta Mountains by enhancing precipitation in the western end of the range (Munroe and Mickelson, 2002; Munroe et al., 2006).

During the LGM, the western end of the Uinta Mountains was occupied by the Western Uinta Ice Field (Refsnider, 2007; Oviatt, 1994; Fig. 1a). This pattern of glaciation is unique to the western part of the range; farther to the east, summit elevations and topographic relief increase, but glaciers were confined to individual valleys. Distributary glaciers flowed from the Western Uinta Ice Field north into the Bear River drainage (Munroe, 2005), west into the Weber (Oviatt, 1994) and Provo River drainages (Refsnider, 2007), and south into the North Fork of the Duchesne and Rock Creek drainages (Laabs and Carson, 2005).

The west end of the range is an ideal location to further investigate the hypothesis that the influence of Lake Bonneville, 60 to 90 km upwind (west) of the Western Uinta Ice Field, resulted in enhanced precipitation and more positive glacier mass balances in the western Uinta Mountains during the LGM. If this hypothesis is correct, we would expect that (1) glaciers flowing from the Western Uinta Ice Field remained at or near their maximum extent later than glaciers in nearby mountain ranges not adjacent to Lake Bonneville, and (2) the western-most glaciers in the range reflected a greater dependence on increased LGM precipitation than did glaciers farther east in the range. To test the hypothesis, we used cosmogenic ^{10}Be and ^{26}Al surface-exposure dating to determine the age of moraine boulders and striated bedrock surfaces in the Provo River drainage. Additionally, we used a physically-based, 2-D numerical glacier model (cf. Plummer and Phillips, 2003) for simulating changes in the extent of the Western Uinta Ice Field under different climate scenarios to make inferences about the local climate during the LGM.

Methods

Cosmogenic nuclide surface-exposure dating

To constrain the timing of the LGM in the western end of the Uinta Mountains, we collected rock samples for surface-exposure dating from the tops of boulders on the crest of the outermost lateral/end moraine in the North Fork of the Provo River Valley, which is south of the former ice divide (Figs. 1a and c). With one exception (NFP-13), all samples came from boulders at least 60 cm in height. All samples are weakly-metamorphosed quartz-rich sandstone or quartzite. Six of the twelve samples came from surfaces with glacial polish and/or striations, which indicate that virtually no surface erosion has taken place since deposition.

To estimate the timing of deglaciation in the western end of the range, we collected samples for cosmogenic ^{10}Be and ^{26}Al measurement from striated, moderately-metamorphosed quartz sandstone bedrock at Bald Mountain Pass (Fig. 1d), located below the former ice divide. For all samples, beryllium and aluminum were extracted from 35 to 50 g of clean quartz and chemically isolated in the University of Wisconsin - Madison Cosmogenic Nuclide Preparation Lab following the methods of Bierman et al. (2002) and Kaplan et al. (2004). ^{10}Be/^{9}Be and ^{26}Al/^{27}Al ratios were measured at the Purdue Rare Isotope Measurement Lab using accelerator mass spectrometry (AMS; Muzikar et al., 2003).

We calculated local ^{10}Be and ^{26}Al production rates using sea-level high-latitude production rates of 5.1±0.3 and 31.1±0.9 atoms g SiO_2^{-1} yr^{-1}, respectively, and the altitude and latitude scaling equations of Stone (2000). Scaling factors were calculated for sample thickness and topographic shielding according to Gosse and Phillips (2001) and Dunne et al. (1999), respectively; attenuation length values used are from Brown et al. (1992). Because half of the boulders and all bedrock surfaces sampled have preserved glacial polish or striations, we assume only minimal erosion (<1 cm) during exposure history, and the effect of this on exposure age is negligible (Bierman et al., 1999). Potential effects of moraine stabilization and degradation are addressed in Discussion. The effect of possible shielding by snow cover is not included in surface-exposure age calculations because of large uncertainties in the depth and duration of snow cover on moraine boulders since deposition. However, moraines form topographic high points in the landscape and are likely windswept of snow where vegetation is sparse; we therefore suspect that snow cover atop the sampled boulders has had a minimal effect on production rates of cosmogenic nuclides. The effects of prolonged snow cover on bedrock surfaces at Bald Mountain Pass are likely more significant and are discussed below. Temporal changes in the intensity of the geomagnetic field and position of the geomagnetic dipole axis affect the intensity of cosmic-ray flux at the Earth's surface and thus affect cosmogenic nuclide production rates, but for surfaces exposed for less than 20 ka at mid-latitudes, such effects are minor (Kubik et al., 1998; Licciardi et al., 1999), and we applied no correction. Uncertainties in exposure age, reported here at 2σ, include analytical uncertainties in AMS measurements and analytical blank corrections for both beryllium and aluminum, as well as uncertainties in ICP-AES measurements for aluminum (Tables 3 and 4).

Glacier modeling

Glacial deposits in the North Fork Provo drainage are exceptionally well preserved, and lateral and end moraines

https://doi.org/10.1016/j.yqres.2007.10.014 Published online by Cambridge University Press

clearly mark the LGM ice extent (Refsnider et al., 2007). The areal extent of LGM glaciers elsewhere in the western Uintas has been documented by Oviatt (1994), Munroe (2005), Laabs and Carson (2005) (Fig. 1a). Of particular interest to us is the Western Uinta Ice Field, which formed over the far western end of the range (Figs. 1a and b). To provide a means of examining many different combinations of temperature and precipitation across this region with varying precipitation, we applied a numerical model developed by Plummer and Phillips (2003), and from this, we can make inferences about climate in the western Uinta Mountains during the LGM based on reconstructed LGM ice extents. This 2-D, physically-based approach, previously applied to several drainages in the Uintas and Wasatch Range by Laabs et al. (2006), is comprised of (1) a 2-D surface energy- and mass-balance model that calculates net annual accumulation/ablation of ice in a drainage basin and (2) a 2-D ice flow model that simulates the formation of steady-state glaciers based on prescribed net annual accumulation/ablation computed in the mass/energy-balance model. This forward modeling approach calculates a 2-D glacier distribution directly from a prescribed climate, thus eliminating the need to estimate ELAs from accumulation–area ratios or other similar methods to make interpretations about paleoclimate.

The energy- and mass-balance component of the model determines net annual ice accumulation/ablation for each grid cell in a digital elevation model (DEM) by tracking the monthly accumulation and ablation through several years until the annual result is constant. The melt rate calculations include short- and long-wave radiation exchanges, turbulent energy exchanges, and advective energy exchanges with the snow surface. Primary climate data inputs are modern precipitation and temperature, which have the largest impact on annual glacier mass balance (Paterson, 1994). Secondary inputs include wind speed, relative humidity, cloudiness, and the standard deviation of mean daily temperature. Based on the results of the energy- and mass-balance model, the steady-state distribution of ice thickness is calculated using a 2-D, in-the-horizontal-plane, finite-difference flow model. The ice flux between cells is a function of ice thickness (*H*) and shear stress (τ), and the average horizontal flow velocity, u, integrated over H, is the sum of the sliding and deformation components of velocity, u_s and u_d, respectively:

$$u = u_s + u_d = f(\tau B)^n + (1-f)H\frac{2}{5}(\tau A)^m \quad (1)$$

where f is a factor controlling the ratio of sliding to deformation, A and B are coefficients of sliding and deformation, respectively, H is the ice thickness, ô is the basal shear stress, and the values of n and m used are 2 and 3, respectively, taken from Fastook and Chapman (1989). The ratio of sliding to deformation, f, used here was 0.5, and values used for A and B were 1.0×10^{-7} yr^{-1} Pa^{-3} and 1.5×10^{-3} m yr^{-1} Pa^{-2} taken from Plummer and Phillips (2003).

Climatic inputs for application of the model were derived from 13 weather stations within or proximal to the western Uinta Mountains with continuous records spanning the 1989–2004 hydrologic years (Table 1). Vertical precipitation gradients differ between valleys in the western end of the range (Laabs et al., 2006), because the eastern part of the study area is affected by

Table 1
Sources of modern climate data

Station Name	Fig. 4.1	Lat., °N	Long., °W	Elevation, m	Source*
Trial Lake	a	40°41′	110°57′	3037	SNOTEL
Kamas	–	40°39′	111°17′	1981	WRCC
Beaver Divide	b	40°37′	111°6′	2524	SNOTEL
Chalk Ck #1	c	40°51′	111°3′	2774	SNOTEL
Chalk Ck #2	d	40°54′	110°4′	2500	SNOTEL
Smith and Morehouse	e	40°47′	111°7′	2317	SNOTEL
West-Fork Hanna	f	40°28′	110°58′	2561	RAWS
Hanna	–	40°14′	110°58′	2064	WRCC
Lily Lake	g	40°52′	110°48′	2759	SNOTEL
Hayden Fork	h	40°48′	110 53′	2774	SNOTEL
Lakefork Basin	i	40°44′	110°37′	3323	SNOTEL
Rock Creek	j	40°33′	110°42′	2409	SNOTEL
Evanston	–	40°16′	110°58′	2183	WRCC

*SNOTEL= Snowpack Telemetry; WRCC=Western Regional Climate Center; RAWS= Remote Automated Weather Station. All data are available from www.wrcc.dri.edu.

Table 2
Monthly mean climate data

Month	Temperature (°C)	Daily Temp. Stan. Dev. (°C)	Temperature Lapse Rate (°C/m)	R^2	Cloudiness (%)	Relative Humidity	Wind Speed (m/s)
October	3.73	4.75	$y=-0.0057x+18.36$	0.88	0.3	0.56	2
November	−3.10	4.91	$y=-0.0051x+9.95$	0.82	0.4	0.61	2
December	−6.76	4.94	$y=-0.0037x+2.83$	0.63	0.4	0.61	2
January	−6.49	4.63	$y=-0.0035x+2.53$	0.64	0.4	0.59	2
February	−5.69	4.93	$y=-0.0051x+7.60$	0.70	0.4	0.54	2
March	−1.75	4.29	$y=-0.0050x+11.28$	0.70	0.4	0.48	2
April	1.93	4.98	$y=-0.0055x+16.00$	0.62	0.4	0.40	2
May	6.52	4.09	$y=-0.0060x+21.90$	0.74	0.4	0.40	2
June	11.06	3.71	$y=-0.0067x+28.32$	0.84	0.2	0.39	2
July	15.01	2.55	$y=-0.0064x+31.63$	0.80	0.2	0.43	2
August	14.30	2.39	$y=-0.0061x+30.16$	0.85	0.2	0.49	2
September	9.59	4.01	$y=-0.0057x+24.43$	0.91	0.3	0.53	2

https://doi.org/10.1016/j.yqres.2007.10.014 Published online by Cambridge University Press

Table 3
^{10}Be data boulder surface exposure ages from the North Fork Provo Moraine

Sample	Elevation (m asl)	Latitude (°N)	Longitude (°W)	Striated and/or polished	Boulder height (cm)	Sample thickness (cm)	Scaling factor[a]	^{10}Be/^{9}Be (10^{-15})	2σ Uncertainty	^{10}Be 10^4 atoms g^{-1} SiO_2	2σ Uncertainty	Age (ka)
NFP-1	2319	40°35.911′	111°5.654′		76	5	26.57	335[b]	16	32.2	1.6	12.2
NFP-2B	2327	40°42.137′	111°5.669′	yes	69	3	27.24	462[b]	16	43.5	1.5	16.0
NFP-3A	2321	40°42.121′	111°5.622′	yes	189	6	26.42	402[b]	43	48.1	5.2	18.3
NFP-4A	2324	40°35.775′	111°5.562′		125	5	26.63	723[c]	20	47.3	1.3	17.8
NFP-4B	2324	40°35.775′	111°5.562′	yes	155	2.5	27.25	386[b]	19	39.1	1.9	14.4
NFP-4C	2324	40°35.775′	111°5.562′		83	3	27.13	366[b]	18	37.5	1.9	13.9
NFP-4D	2324	40°35.775′	111°5.562′		66	3	27.12	795[c]	38	53.3	2.6	19.7
NFP-5	2346	40°35.677′	111°5.222′	yes	157	3.5	27.41	426[b]	16	44.6	1.7	16.3
NFP-12	2505	40°36.037′	111°4.312′		60	6	29.70	761[c]	23	49.3	1.5	16.7
NFP-13	2504	40°36.044′	111°4.305′		45	4.5	30.08	778[c]	23	51.1	1.5	17.0
NFP-14	2489	40°36.017′	111°4.395′	yes	75	3	30.19	803[c]	22	54.2	1.5	18.0
NFP-15	2471	40°35.975′	111°4.517′	yes	110	2.5	29.98	780[c]	26	53.7	1.8	18.0

[a] Calculated in accordance with Stone (2000); accounted for topographic shielding and sample thickness.
[b] Measured relative to NIST standard SRM 4325 and corrected based on a chemical blank with a ^{10}Be/^{9}Be ratio $1.78\times10^{-14}\pm2.40\times10^{-15}$.
[c] Measured relative to NIST standard SRM 4325 and corrected based on a chemical blank with a ^{10}Be/^{9}Be ratio $1.50\times10^{-14}\pm2.50\times10^{-15}$.

summer monsoonal moisture, and the western part receives a disproportionate amount of snow at moderate elevations due to orographic effects on east-moving Pacific air masses (Mitchell, 1976). These differences complicate interpretation of paleo-ELAs because the modern ELA may also vary along the strike of the range. The modeling approach employed here obviates that concern, assuming that the spatial distribution of climatic inputs can be reliably represented. In addition, the presence of the Western Uinta Ice Field during the LGM means that ice production in one drainage contributed an unknown ice flux to neighboring drainages. The ice flow model should appropriately distribute those fluxes if, again, the spatial description of the climatic controls on glacier production are adequate.

To describe the modern vertical and areal distribution of precipitation across the modeling domain, we derived monthly precipitation grids with a resolution of 750 m using the data from the meteorological stations included in Table 1. A variety of statistical and geostatistical methods have been used for the spatial interpolation of precipitation data in regions with widely-spaced monitoring stations (e.g., Daly et al., 1994; Goovaerts, 2000; Diodato, 2005). In general, for regions with complex terrain where precipitation amounts increase with elevation, estimates of precipitation taking into account elevation data are more accurate than estimates using precipitation data alone (Goovaerts, 2000; Diodato, 2005). We constructed monthly precipitation grids by 3-D inverse-distance interpolation of the precipitation data from 13 weather stations using 20 layers in the vertical direction and then linearly interpolating the result to the DEM surface. Monthly precipitation grids are shown in Fig. 2 in the supplementary materials.

In an attempt to evaluate the relative accuracy of the monthly precipitation distributions we developed, we compared mean annual stream discharge data from the Weber, Bear, and Provo Rivers (Fig. 1a) to the predicted mean annual precipitation in each basin. These are the only streams in the modeling domain with suitable discharge data for such an analysis. Assuming that

Table 4
^{10}Be and ^{26}Al data and bedrock surface-exposure ages from Bald Mountain Pass

Sample	Elevation (m asl)	Latitude (°N)	Longitude (°W)	Sample thickness (cm)	^{10}Be scaling Factor[a]	^{26}Al Scaling Factor[a]	^{10}Be/^{9}Be (10^{-15})[b]	2σ Uncertainty[b]	^{26}Al/^{27}Al (10^{-15})[c]	2σ Uncertainty[c]
BMP-2	3277	40°41.391′	110°53.955′	5	49.09	300.48	1033	29	1140	90
BMP-4	3280	40°41.374′	110°53.999′	4	48.30	295.99	1051	23	1360	71
BMP-5	3250	40°41.206′	110°54.517′	2.5	48.16	294.88	1215	230	733	42
BMP-7	3250	40°41.242′	110°54.565′	3	47.96	293.71	1124	41	1110	90

Sample	^{10}Be 10^4 atoms g^{-1} SiO_2	2σ Uncertainty	^{26}Al 10^4 atoms g^{-1} SiO_2	2σ Uncertainty	^{26}Al/^{10}Be	2σ Uncertainty	^{10}Be Age (ka)	2σ Analytic Uncertainty	^{26}Al Age
BMP-2	67.8	1.9	402.8	42.2	5.94	1.29	13.8	0.8	13.5
BMP-4	68.5	1.5	382.9	33.0	5.59	0.99	14.2	0.6	13.0
BMP-5	77.6	14.7	364.1	32.6	4.69	1.97	16.2	6.1	12.4
BMP-7	72.9	2.7	384.4	40.8	5.27	1.18	15.3	1.1	13.2
				Weighted mean=			14.3	0.5	13.0

[a] Calculated in accordance with Stone (2000); accounted for topographic shielding and sample thickness.
[b] Measured relative to NIST standard SRM 4325 and corrected based on a chemical blank with a ^{10}Be/^{9}Be ratio $1.50\times10^{-14}\pm2.50\times10^{-15}$.
[c] Corrected based on a chemical blank with a ^{26}Al/^{27}Al ratio $1.00\times10^{-17}\pm9.00\times10^{-15}$.

https://doi.org/10.1016/j.yqres.2007.10.014 Published online by Cambridge University Press

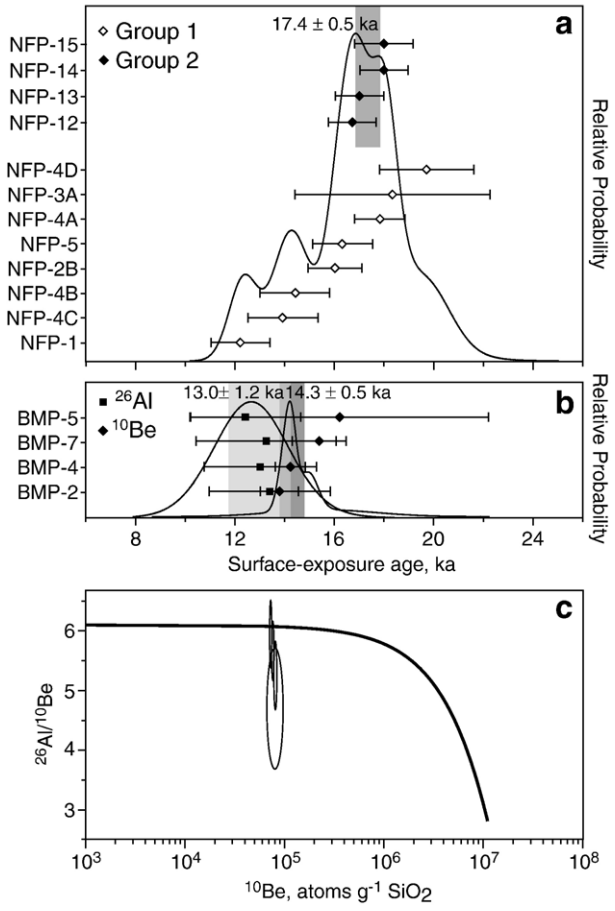

Figure 2. ^{10}Be and ^{26}Al surface-exposure ages and relative probability curves for boulders on the North Fork Provo (NFP) end moraine (a) and striated bedrock at Bald Mountain Pass (BMP) (b). In (a), NFP Group 1 includes ages from the frontal moraine, and NFP Group 2 includes ages from the lateral moraine (Fig. 1c). Error bars show 2σ analytical uncertainty, and the grey box shows the error-weighted mean for the Group 2 ages. In (b), the darker grey boxes show error-weighted mean ages for each ^{10}Be dataset, including 2σ uncertainty. The lighter grey box in the BMP dataset shows the error-weighted mean age for the ^{26}Al data, and error bars again show the 2σ uncertainty. (c) Cosmogenic ^{10}Be concentration versus ^{26}Al/^{10}Be ratio for samples taken from striated bedrock at Bald Mountain Pass. Note that the error ellipses show 1σ analytical uncertainty. The solid curve shows the continuous exposure trajectory. The steady-state erosion curve forming the lower boundary of the steady-state erosion envelope (Lal, 1991) is not shown because the samples exhibit well-preserved glacial polish and striations. At a 1σ analytical uncertainty, two of the four samples plot below the continuous exposure curve, indicating complex burial histories (see text for further discussion).

the conditions controlling the balance between precipitation and evapotranspiration in each basin are similar, the ratio of mean annual stream discharge to predicted mean annual net precipitation in each basin should be approximately equal. We used a 15-year record (1989–2004) of U.S. Geological Survey discharge data from stream gages and calculated mean annual precipitation in each basin from our interpolated monthly precipitation grids. The ratios of stream discharge to precipitation for the three basins were 0.51, 0.43, and 0.55, respectively. While the first and last of these values are within 10% of one another, the coefficient calculated for the Bear River drainage is considerably lower, suggesting either that our model underpredicts precipitation in that basin or that the runoff coefficient for that basin is actually much lower than in the other drainages.

Denser vegetation in the upper Bear River watershed and across the north slope of the range may be at least partially responsible for the apparent lower runoff coefficient in that valley. It is possible, however, that our interpretation of the precipitation data overestimates precipitation in that basin. The Bear River RAWS meteorological station, one of three meteorological stations in that drainage, consistently reported anomalously low daily precipitation values compared to the two other stations and was therefore excluded from our calculation of precipitation distribution. Precipitation data from that station are approximately half that of the Lily Lake SNOTEL station (Table 1), located only 2 km upvalley, and very similar to precipitation measurements at the Evanston WRCC station, approximately 40 km to the north and 500 m lower in elevation. Because the anomalous precipitation measurements and the lower stream discharge ratio both come from the Bear River drainage, we place less confidence in the accuracy of the interpolation in this valley, and thus, a higher uncertainty on the simulation results for the Bear River Glacier. We believe that the interpolations describe modern precipitation in other drainages of the western end of the range more accurately.

The relatively sparse distribution of meteorological stations in the western Uinta Mountains does not allow for the calculation of temperature lapse rates specific to each valley, so we instead compiled the 1989–2004 temperature data from the 13 stations listed in Table 1 and computed monthly mean least-squares linear-regression fits for the entire model domain (Table 2). Other necessary climate input parameters, including mean monthly humidity, wind speed, and cloudiness, are only monitored at few weather stations in and near the study area. There are no significant relationships between these parameters and elevation in the available data for the Uinta Mountains (Laabs et al., 2006), so values for these parameters were kept constant with elevation (Table 2).

Plummer and Phillips (2003) first applied the glacier model to simulate glaciers in the Bishop Creek watershed in the Sierra Nevada, and after tuning several of the energy-balance parameters, the predicted extent of contemporary glaciers agreed well with the observed ice extent. Since no glaciers exist in the Uintas today, a different approach for evaluating the energy-balance parameters is necessary. In this study, we used aerial photographs from August of 1993 to identify 10 non-perennial snow fields remaining from the relatively wet preceding winter. The energy-balance model input was adjusted to account for the slightly cooler and wetter conditions from the 1993 hydrologic year (1.22× wetter, 1.1°C cooler than the 1989–2004 means), and areas of predicted positive mass balance and ablation minima were compared to the observed snow packs (Refsnider, 2006).

Tuning the model to make simulated snow distributions match observed snow distributions could be accomplished by manipulation of many variables, including, for example, the albedo for snow, local wind speed, or the turbulent heat transfer coefficient. In general, however, the model is much more sensitive to albedo than to other parameters, because albedo has a

https://doi.org/10.1016/j.yqres.2007.10.014 Published online by Cambridge University Press

direct impact on shortwave radiation, the largest component of the surface energy balance. The albedo of paleoglaciers is relatively uncertain because there are no reliable means to estimate how much debris was incorporated into the ice or to assess other factors controlling albedo. Because of the sensitivity to albedo and its associated uncertainty, we chose to adjust only this parameter in attempts to match observations. Using this approach, the best agreement was reached when values for the low and high albedo parameters, which are used for ice and snow-covered grid cells, respectively, were 0.40 and 0.75. These values are well within ranges observed on modern glaciers (Paterson, 1994; Oerlemans and Knap, 1998), and the fact that simulated wet-year snowpack distribution approximately matches the (albeit sparse) observations gives us some confidence that the model reasonably approximates actual net ablation.

Using the calibration parameters described above, we applied the model to the entire extent of the Western Uinta Ice Field using a grid resolution of 750 m for the net annual snow accumulation calculations and 360 m for the ice-flow model. We also applied the model to Swifts Canyon (Fig. 1a), which was occupied by a 6-km-long glacier during the LGM (Oviatt, 1994), using a 60-m grid resolution for the ice-flow model. The ice flow model was run until the growth of glaciers reached a steady-state thickness and extent. The addition of glaciers and ice fields to the landscape results in a considerable alteration in the surface energy and mass balance, as noted by Plummer and Phillips (2003). For alpine glaciers, increasing the effective elevation of the valley floor reduces topographic shading, which increases the energy available for melting. However, such an elevation change also results in slightly cooler temperatures and increased precipitation at the ice surface. Laabs et al. (2006) found these two effects more or less balanced out for the three glaciers they simulated. For the Western Uinta Ice Field, however, there was virtually no reduction in topographic shading as the ice thickness increased, so the temperature and precipitation changes do not balance one another. To account for these effects, we used an iterative approach, recalculating the mass and energy balance for the new, ice-covered terrain surface and then rerunning the ice flow model. To adjust for the increase in precipitation with elevation, we constructed a mean precipitation gradient grid by dividing the slope of each precipitation grid by the slope of the DEM grid. The precipitation gradient grid, with a resolution of 750 m, was then multiplied by the ice thickness grid, and the result was added to each monthly grid. For the glaciers flowing from the Western Uinta Ice Field, 3–4 iterations were sufficient for the modeled glaciers to reach steady-state, and for the Swifts Canyon Glacier, two iterations were sufficient.

Results

Cosmogenic nuclide surface-exposure dating

Cosmogenic ^{10}Be surface-exposure ages from 12 boulders, 6 of which were polished and/or striated (Table 3), on the crest of the outermost end/lateral moraine at the mouth of the North Fork Provo Valley (Table 3 and Fig. 1c) span a broad range from 12.2±1.2 to 19.7±1.9 ka (±2σ analytical uncertainty; Fig. 2a). Boulder samples were collected from two different areas on the moraine. Samples in Group 1 were collected from boulders on distal side of the crest of the frontal moraine near the center of the valley (Fig. 1c). Here the moraine has a relatively broad crest, and in some areas, appears to be a composite feature more than 20 m wide with low-relief hummocky topography. Samples in Group 2 are from boulders situated along the southeastern part of the ridge where it becomes a lateral moraine (Fig. 1c). The crest along this section of the moraine is only a few meters wide, and the sampled boulders were located along the center of the crest. The eight Group 1 samples exhibit a broad spread in ages, ranging from 12.2±1.2 to 19.7±1.9 ka. The four Group 2 samples cluster much more tightly between 16.7±1.0 and 18.0±1.2 ka, with an error-weighted mean of 17.4±0.5 ka.

^{10}Be and ^{26}Al data and surface-exposure ages from four samples collected from striated bedrock at Bald Mountain Pass (Fig. 1d) are given in Table 4. ^{26}Al ages range from 12.4±2.2 to 13.5±2.8 ka and have an error-weighted mean of 13.0±1.2 ka; ^{10}Be ages range from 13.8±0.8 to 16.2±6.1 ka and have an error-weighted mean of 14.3±0.5 ka (Fig. 2b). Though weighted-mean ^{10}Be and ^{26}Al exposure ages overlap at 2σ, the ^{26}Al ages are 3–23% younger than the ^{10}Be ages from the same samples, and ^{26}Al/^{10}Be ratios range from 4.7±2.0 to 5.9±1.3 (Fig. 2c).

We investigated the potential effects of snow shielding on surface-exposure ages using the method of Gosse and Phillips (2001), and assuming one meter of snow cover for 4 months annually, the error-weighted mean ages increase by 3% and 10% for the North Fork Provo terminal moraine and Bald Mountain Pass bedrock surfaces, respectively.

Glacier modeling

Many combinations of changes in climatic variables can produce glaciers that match the LGM glacial extent in each basin of the western Uintas. Figure 3 shows the output for one such simulation using a temperature depression of 6°C and 2× (i.e., a doubling of) modern precipitation. Note that the ice extent in the North Fork Duchesne, Rock Creek, and Bear River drainages is close to the mapped ice limit, but the Main Weber Glacier is too large, and virtually no ice has accumulated in the Provo River drainage. To examine differences among the climatic conditions necessary to reproduce glaciers across the western end of the Uintas, we identified for each basin in the domain the specific combinations of temperature and precipitation change for which the modeled LGM ice extent matched the observed LGM extent (Figs. 4 and 5). To properly account for ice flow across topographic divides, the reported precipitation and temperature combinations are based on simulations run for the entire domain of the ice field. The values of ice flow parameters A and B (Eq. (1)) can be tuned so that modeled ice thickness better matches observed ice thickness based on geomorphic evidence. Modeled ice thicknesses for the Western Uinta Ice Field were consistent with reconstructed ice thickness when we prescribed values of

https://doi.org/10.1016/j.yqres.2007.10.014 Published online by Cambridge University Press

$A = 1.0 \times 10^{-7}$ yr^{-1} Pa^{-3} and $B = 1.5 \times 10^{-3}$ m yr^{-1} Pa^{-2}. These values fall within the range of empirically determined values for mountain glaciers (cf. Laabs et al., 2006).

The resulting temperature–precipitation curves constructed for each glacier are plotted in Figure 4 and are discussed below.

Discussion

Cosmogenic nuclide surface-exposure dating

North fork Provo terminal moraine

We calculate landform ages using an inverse-variance weighted mean of cosmogenic surface-exposure ages, which incorporates analytic uncertainty into the age uncertainty, in Isoplot 3.00 (Ludwig, 2003). For moraines, we interpret the weighted mean as a minimum limiting age for when the glacier margin retreated from the location of the moraine. The age distribution for Group 1 samples from the North Fork Provo terminal moraine (Fig. 2a) clearly shows that the frontal part of the moraine has undergone a long period of stabilization following deposition, with younger ages coming from boulders that were more recently overturned or exhumed (Hallet and Putkonen, 1994; Zreda et al., 1994; Putkonen and Swanson, 2003). The broad area of low-relief, hummocky topography along this frontal part of the moraine is more than 20 m wide at the crest is also suggestive of a period of post-glacial moraine stabilization. The oldest boulder (NFP-4D) has an age of 19.7±1.9 ka, which, assuming this boulder had no inherited ^{10}Be, suggests that the outermost part of the compound moraine was forming by this time. However, the Group 1 age distribution does not allow for a straightforward interpretation of the age of the moraine.

The samples in Group 2 (Fig. 2a) came from 1 to 1.5 km up valley from the frontal moraine where the lateral moraine is a sharp-crested feature with very little evidence of post-depositional erosion. The exposure age of the four boulders in Group 2 cluster tightly around a weighted mean age of 17.4±0.5 ka. We contend that these samples provide a more reliable estimate for the age of the moraine than do the ages from Group 1 samples. According to this interpretation, the glacier likely abandoned the moraine by 17.4±0.5 ka. If the youngest exposure age in Group 1 is from a boulder exhumed during a period of post-depositional moraine surface instability, the moraine may have taken approximately 5 ka to stabilize as buried ice slowly melted to form the area of hummocky topography.

Bald mountain pass

The surface-exposure age of the polished and striated quartzite bedrock at Bald Mountain Pass can theoretically be used to provide a limit on the timing of deglaciation in the western Uinta Mountains. Ice with a thickness of nearly 300 m occupied the pass during the LGM, and indicators of ice flow direction show that ice flowed northward through the pass for at

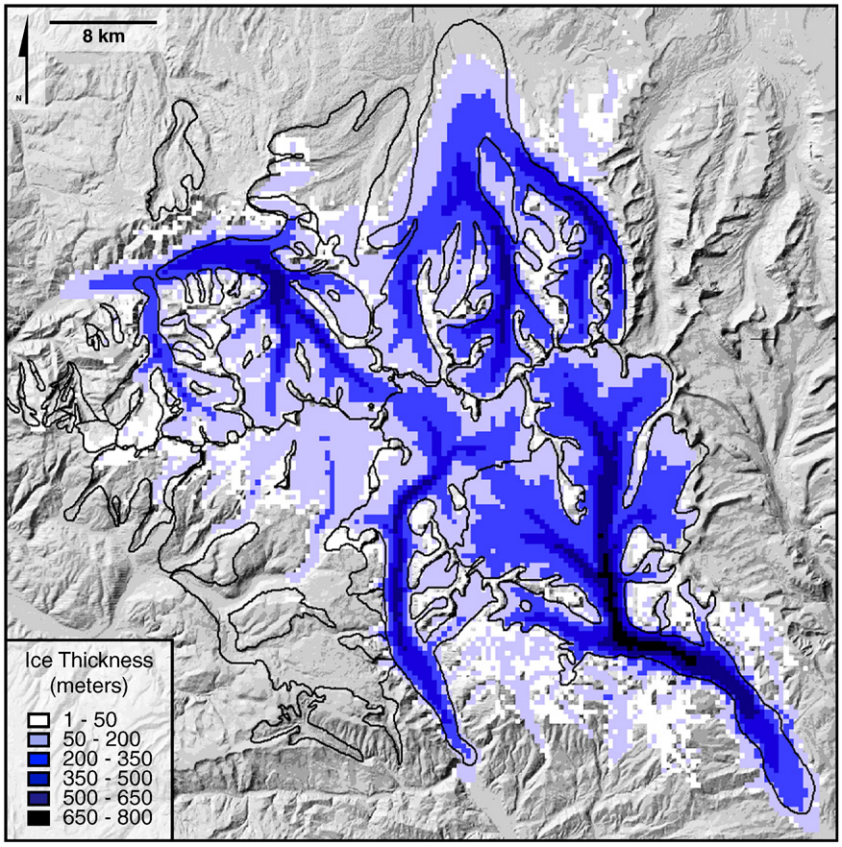

Figure 3. Model results for a temperature depression of 6°C and 2× modern precipitation. The solid black lines denote LGM ice margins based on geomorphic evidence. Note that the termini of most glaciers, primarily those in the eastern and northern part of the model domain are near or beyond their mapped extent, yet glaciers in the southwestern part of the domain have not advanced out of the cirque basins.

https://doi.org/10.1016/j.yqres.2007.10.014 Published online by Cambridge University Press

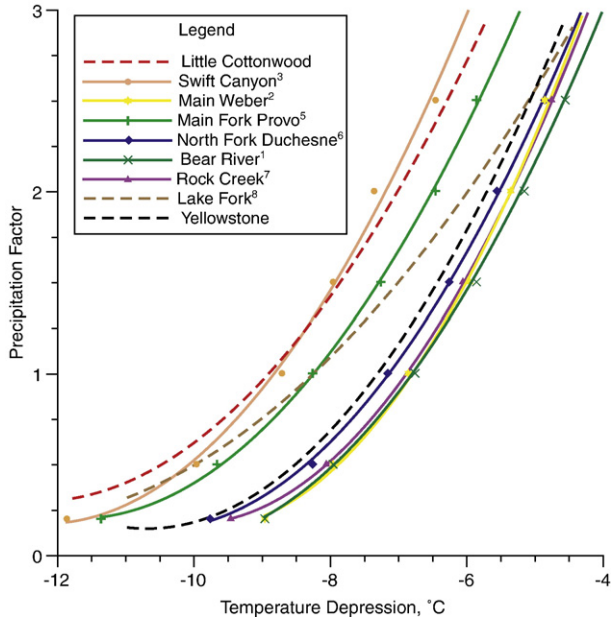

Figure 4. Curves representing temperature and precipitation combinations resulting in modeled glacier extents matching observed LGM glacier extents based on geomorphic evidence. A precipitation factor of 1 represents modern precipitation. Superscripted numbers after the glacier names in the legend refer to the glacier numbering scheme used in Figure 1a. Dashed curves are from Laabs et al. (2006); the Lake Fork and Yellowstone Glaciers were immediately east of the Rock Creek outlet of the Western Uinta Ice Field on the southern slope of the Uinta Mountains (Fig. 1a), and the Little Cottonwood Glacier was on the western slope of the Wasatch Range in Little Cottonwood Canyon.

least the latest part of the LGM (Atwood, 1909; Oviatt, 1994; Refsnider, 2007). ^{10}Be surface-exposure ages of the four bedrock samples collected at Bald Mountain Pass have an error-weighted mean of 14.3±0.5 ka (Fig. 2b). The ^{26}Al surface-exposure ages for the same samples have a weighted-mean age of 13.0±1.2 ka. ^{26}Al/^{10}Be ratios range from 4.7±2.0 to 5.9±1.3 (Fig. 2c; note that the error ellipses in Figure 2c show 1σ uncertainties). The disparity between the ^{26}Al and ^{10}Be ages for all samples other than BMP-4 cannot be explained by appealing to snow or sediment shielding, because with such low ^{10}Be concentrations and with ^{26}Al/^{10}Be ratios of 4–5, the samples would have required 200–600 ka of burial following an exposure period of an order of magnitude less duration (*cf.* Bierman et al., 1999). Previous studies have shown that striated bedrock can contain inherited nuclides due to relatively minor amounts of bedrock abrasion (less than 3 m) by glacier ice (e.g., Briner and Swanson, 1998; Colgan et al., 1998). An outcrop of shale exposed at the highest part of Bald Mountain Pass suggests that in some areas, subglacial erosion at the pass during the last glaciation was relatively inefficient and was likely not sufficient to remove the prior inventory of cosmogenic nuclides from quartzite bedrock.

The uncertainty in the ^{26}Al/^{10}Be ratios for all four samples from Bald Mountain Pass overlaps with the constant-exposure curve at 2σ due to relatively large uncertainties in the ^{26}Al AMS measurements. However, at 1σ uncertainty, only BMP-2 and BMP-4 overlap with the constant-exposure curve (Fig. 2c). This suggests that there was likely sufficient glacial erosion during the last glaciation to remove any previously-acquired cosmogenic nuclides in at least these two samples. Samples BMP-5 and BMP-7, which only overlap with the constant-exposure curve at 2σ were collected from bedrock surfaces located within a few hundred meters of the reconstructed ice divide (Refsnider et al., 2007) and within 200 m of the base of Bald Mountain. Lower basal sliding rates at these sampling sites would result in lower erosion rates and thus could result in an inherited nuclide signal,

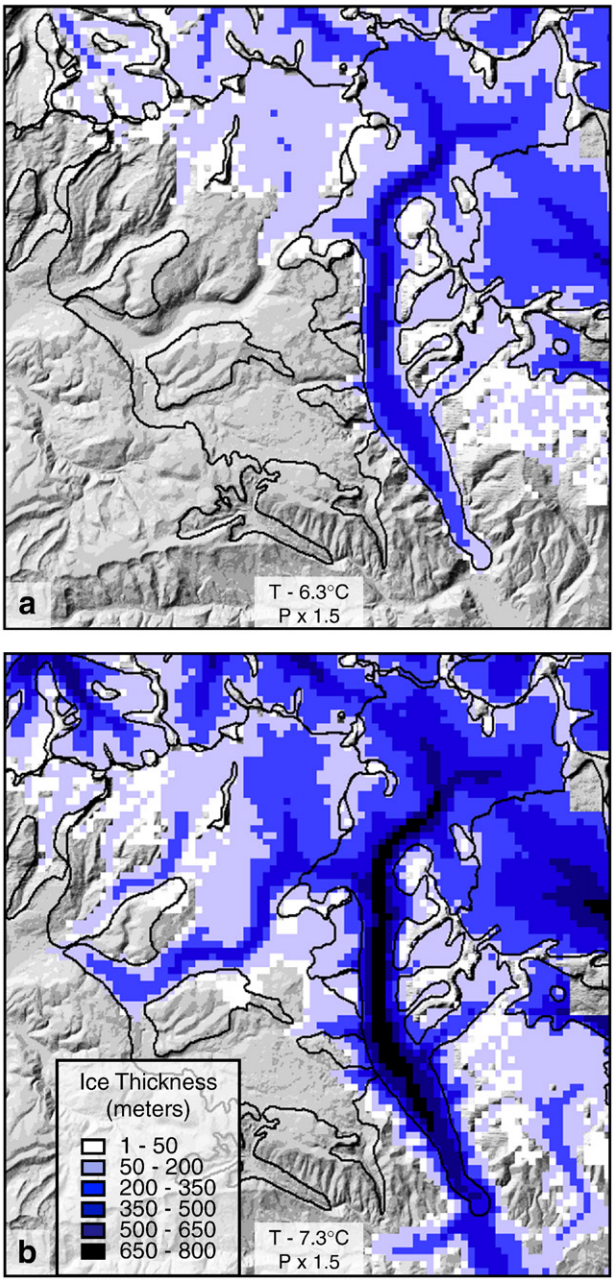

Figure 5. Model results for the Main Fork Provo and North Fork Duchesne glaciers. The black lines denote LGM ice margins based on geomorphic evidence. (a) With a temperature depression of 6.3°C and a 50% increase in precipitation, the simulated North Fork Duchesne Glacier matches its mapped thickness and extent. (b) The simulated Main Fork Provo Glacier required an additional 1°C of cooling or an additional 25% increase in precipitation to reach its mapped extent. Under these cooler/wetter conditions, the ice in the North Fork Duchesne valley extends well beyond its mapped extent.

https://doi.org/10.1016/j.yqres.2007.10.014 Published online by Cambridge University Press

which would cause the sample $^{26}Al/^{10}Be$ ratios to plot below the constant-exposure curve in Figure 2c. For this reason, we do not feel the $^{26}Al/^{10}Be$ ratios of samples BMP-5 and BMP-7 necessarily reflect the timing of the deglaciation of Bald Mountain Pass, and we do not include them in our estimate of the timing of deglaciation of the pass.

The weighted mean of the ^{26}Al and ^{10}Be surface-exposure ages for BMP-2 and BMP-4 is 14.0±0.5 ka. Shielding by snow cover is likely an important issue at Bald Mountain Pass, but quantifying the effects of this over the exposure history of the sample is difficult. If we assume the samples were annually covered by 1 m of snow for 4 months, the weighted-mean age increases by approximately 10% to 15.6±0.5 ka. Thus, we interpret the surface-exposure age of 14.0±0.5 ka as a *minimum* estimate of the time of deglaciation of Bald Mountain Pass and the ultimate collapse of the Western Uinta Ice Field.

Ages in a regional context

Munroe et al. (2006) constrained the timing of the LGM in the southwest Uintas with ^{10}Be ages of terminal moraines in the Yellowstone and Lake Fork Canyons. They reported weighted mean ages of 18.0±0.7 and 18.0±1.1 ka for those moraines and suggested that, based on ages from a recessional moraine abutting the Lake Fork terminal moraine, deglaciation did not begin until 16.8±0.7 ka. The weighted-mean age of the North Fork Provo terminal moraine of 17.4±0.5 ka is statistically indistinguishable from the ages of the Lake Fork moraines, located fewer than 50 km to the east (Fig. 6). This suggests that glaciers in the southwestern Uinta Mountains likely all remained at their maximum LGM extents until approximately 16–18 ka.

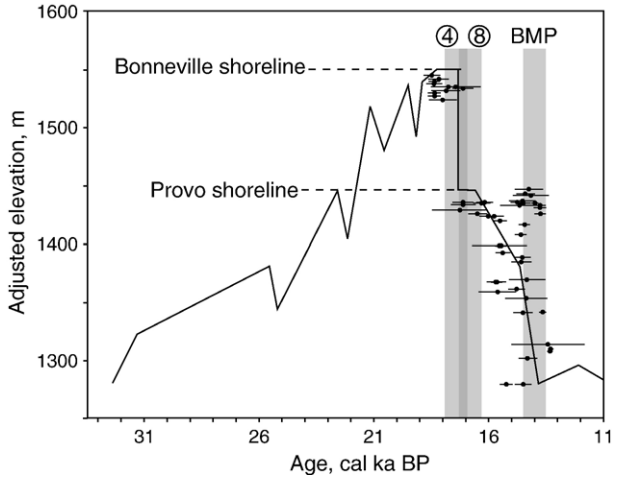

Figure 6. The solid black line shows the Lake Bonneville hydrograph from Oviatt (1997), and the individual data points are from the lake level record from Godsey et al. (2005). All data have been calibrated using CALIB 5.0.2 (Stuiver et al., 2005), and the error bars on the individual data points show the 2σ uncertainty in the ages. Elevations have been adjusted for isostatic rebound of the Bonneville basin. The grey boxes show the 2σ error-weighted means of cosmogenic surface-exposure age datasets. Surface-exposure ages from the North Fork Provo terminal moraine (4), the recessional moraine nested against the terminal moraine in the Lake Fork drainage (8; Munroe et al., 2006), and the striated bedrock at Bald Mountain Pass (BMP). The Bald Mountain Pass data establish a *minimum* estimate for the timing of the collapse of the Western Uinta Ice Field.

The mean boulder-exposure age of the North Fork Provo terminal moraine is slightly younger than moraine ages from nearby ranges to the east. In Colorado, Benson et al. (2004, 2005) dated boulders on LGM terminal moraines in the northern Front Range and central San Juan Mountains using cosmogenic ^{36}Cl, and mean boulder-exposure ages were interpreted to suggest that the onset of deglaciation took place at 18.4 and 18.9 ka, respectively. ^{10}Be boulder-exposure ages from moraines in the Wind River Range in Wyoming are similar in age, ranging from 20.8 to 18.7 ka (Benson et al., 2005; adjusted for the ^{10}Be production rate used here). Comparable exposure-ages with weighted means of 19.6±1.9 and 20.6±2.2 ka have been determined using ^{10}Be and ^{36}Cl, respectively, for boulders on a LGM terminal moraine in the Sawatch Range of central Colorado (Brugger, 2006; Brugger, K.A., personal communication, 2006). These ages, as well as ages from numerous other moraines in the Wind River Range (Gosse et al., 1995; Phillips et al., 1997), all suggest that glaciers in mountain ranges throughout the Middle and Southern Rocky Mountains generally exhibited relatively synchronous behavior with the exceptions of glaciers flowing from the Yellowstone ice cap in Wyoming (Licciardi et al., 2005) and glaciers in the western Uinta Mountains (Munroe et al., 2006).

Munroe et al. (2006) suggest that the onset of retreat of the Lake Fork Glacier at 16.8±0.7 ka (again, note that the uncertainties in the cosmogenic ^{10}Be ages do not include the ca. 6% uncertainty in ^{10}Be production rate (Stone, 2000)) was approximately synchronous with the regression of Lake Bonneville from its high-stand at the Bonneville shoreline and its climate-driven regression from the Provo shoreline at 16.2 to 17.1 cal ka BP (Fig. 6; Oviatt, 1997). Similarly, preliminary ^{10}Be boulder-exposure ages from the Wasatch Range, located between Bonneville basin and the Uinta Mountains, suggest that the Little Cottonwood Glacier remained at its maximum position until 15–17 ka (Lipps et al., 2005). The weighted-mean age of 17.4±0.5 ka for the North Fork Provo moraine suggests that the North Fork Provo Glacier reached its maximum extent at or slightly after the time when Lake Bonneville was at its hydrologic maximum (Fig. 6). Surface-exposure ages from the striated bedrock at Bald Mountain Pass provide another means of comparing the timing of the disappearance of the Western Uinta Ice Field with the regression of Lake Bonneville. The 14.0±0.5 ka weighted-mean age of samples BMP-2 and BMP-4 provides a minimum estimate for the timing of the disappearance of the Western Uinta Ice Field, though incorporating the effects of snow shielding likely increases the age by at least 1000 yr. If this is the case, the collapse of the ice field may have taken place in only 2–3 ka and coincided with the climate-driven regression of Lake Bonneville from the Provo shoreline (Fig. 6), beginning between ca. 16 cal ka BP (Oviatt, 1997) and ca. 14 cal ka BP (Godsey et al., 2005).

Glacier modeling

Response curve trajectories and associated uncertainty

Many different combinations of temperature and precipitation changes can result in a modeled glacier that matches an observed LGM ice extent, so we tested a series of such

https://doi.org/10.1016/j.yqres.2007.10.014 Published online by Cambridge University Press

combinations to explore the range of potential climate scenarios for the LGM. We also modeled the smaller Swifts Canyon Glacier to obtain a temperature–precipitation curve for a glacier that was at the western end of the range but was not connected to the Western Uinta Ice Field.

Temperature–precipitation response curves for the six modeled glaciers follow very similar trajectories, but despite the geographic proximity of the glaciers to one another, no single temperature–precipitation combination reproduced the observed LGM ice extents for all glaciers (i.e., the temperature–precipitation curves in Figure 4 generally do not cross). This suggests that either the input data do not accurately represent modern climate, individual outlet glaciers of the Western Uinta Ice Field responded differently to the same climatic forcing, or temperature or precipitation changes (relative to modern) were not uniform across the western Uinta Mountains during the LGM.

Uncertainty in the modeling results could arise from many different sources, but the largest source is undoubtedly the description of modern climate across the modeling domain. Given the limitations on the model calibrations that can be performed where no modern glaciers or permanent snow fields exist, the availability of modern meteorological data, and on the accuracy of the precipitation interpolations, determining the uncertainties in our description of modern climate and the model calibration is difficult. Uncertainty arising from our method of calibrating the model by adjusting albedo values can only be evaluated by running simulations with altered albedo values. Model simulations run with a low albedo of 0.35 instead of 0.4 resulted in an increase in ice extent and volume similar to that resulting from decreasing temperature by ~0.1°C; reducing the albedo of ice had an effect of similar magnitude. Estimating the amount of supraglacial debris on paleoglaciers is highly speculative, and because there is limited field evidence to suggest that the Western Uinta Ice Field was particularly debris-laden, we contend that our albedo estimates are appropriate. Thus, due to prescribed albedo values, uncertainties of temperature depressions and precipitation factors of less than ±0.2°C and ±~10%, respectively, are likely.

The model is quite sensitive to temperature, and varying the temperature at approximate LGM conditions (5 to 10°C below present; discussed further in the LGM temperature depression section) by more than 0.05°C generally resulted in a significant enough difference in the mass balance that the modeled and observed areal ice extent differed by at least 360 m for the smaller glaciers. However, we are confident that the monthly temperature regressions we used accurately describe the vertical temperature distribution because for 9 of 12 months (including all summer months), elevation alone accounts for at least 70% of the variation in temperature between the 13 meteorological stations from which the data were acquired (Table 2). It is possible that our estimated precipitation distribution includes some error, and substantial errors in the estimation of modern precipitation would bias the results accordingly. For example, if our interpolation uniformly underestimates precipitation by 10%, then our interpretation of LGM climatic conditions with twice modern precipitation would overestimate the necessary temperature depression by less than 0.5°C, with the small Swifts Canyon Glacier being more sensitive than the larger outlet glaciers of the Western Uinta Ice Field. Similarly, overestimating modern precipitation by 10% would result in an estimated LGM temperature depression that is less than 0.5°C too low if precipitation was doubled. Although we have not directly assessed the uncertainty of each temperature–precipitation combination in this study, previous model applications in the Sierra Nevada Range by Plummer (2002) suggest that errors due to limited input data produce uncertainties of temperature depressions and precipitation factors of ±0.5°C and ±30%, respectively. We incorporate this same uncertainty from climate data parameterization in model results presented here.

The model results shown in Figure 4 could also reflect that individual outlet glaciers in the western Uinta Mountains responded differently to the same climatic forcing during the LGM. Using a 1-D ice-flow model, Oerlemans et al. (1998) demonstrated that 12 modern glaciers and ice caps exhibited dramatically different responses to the same prescribed climate forcing, which in their study, was warming. They concluded that glacier hypsometry is an important factor controlling an individual glacier's response to climate change. In the western Uinta Mountains, there is no evidence preserved in the glacial geomorphic record that allows us to easily identify variable responses of modeled glaciers to climate changes during the glaciation, but any variability related to glacier hypsometry and its influence on glacier mass balance is accounted for by the 2-D modeling approach.

With the exception of results for the Main Weber Glacier, the simulated glaciers consistently required increasing precipitation farther west in the range in order to match observed ice extents. For example, if temperatures were reduced by 7°C, the westernmost glaciers (Swifts Canyon and the Main Fork Provo Glaciers) required at least two times modern precipitation, whereas glaciers farther east required no increase in precipitation (Fig. 4). Though there is some uncertainty in the accuracy of the interpolated precipitation grids we applied, a difference of this magnitude in the required variation in precipitation for glaciers across the modeling domain far exceeds the potential error in the precipitation grids. Therefore, we interpret model results to indicate that precipitation varied across the western Uintas during the LGM, as previously suggested by Munroe and Mickelson (2002) and Munroe et al. (2006); the implications of this interpretation for LGM climate inferences are discussed below.

Longitudinal precipitation gradients

Today there exists a strong east–west precipitation gradient across the Uinta Mountains (Munroe and Mickelson, 2002; Laabs et al., 2006). In winter months, the western end receives considerably more precipitation from moist Pacific air masses, but during summer months, precipitation is greatest in the south-central part of the range where the monsoonal moisture regime dominates (Mitchell, 1976). During the LGM, glacier ELAs decreased dramatically toward the western end of the range, but the modern east–west precipitation gradient is not sufficiently steep to completely account for the lower ELAs (Munroe and Mickelson, 2002). Enhanced precipitation in the

https://doi.org/10.1016/j.yqres.2007.10.014 Published online by Cambridge University Press

upwind (western) end of the range due to the influence of pluvial Lake Bonneville has been suggested as a possible mechanism to account for the ELA gradient (Munroe and Mickelson, 2002; Munroe et al., 2006). Based on a modeling approach similar to ours, Laabs et al. (2006) suggested that the difference between modern and LGM climate in the southwestern Uinta Mountains is not the same as the difference between modern and LGM climate in the Wasatch Range. For example, their results suggest that for a temperature depression of ~5°C, glaciers in the Lake Fork and Yellowstone Canyons (Fig. 1a) required an increase in precipitation of 2.5×, whereas the Little Cottonwood Glacier, which advanced to the shoreline of Lake Bonneville, required an increase of 3.5. This difference was attributed to the closer proximity of the Wasatch Range to Lake Bonneville (Laabs et al., 2006).

Our modeling results are, in general, consistent with the hypothesis of a greater east–west precipitation gradient in the Uinta Mountains during the LGM, assuming that the temperature depression in all valleys was uniform and that vertical temperature gradients were similar to modern gradients. The temperature–precipitation curve for Swifts Canyon Glacier, which had one of the lowest ELAs in the Uinta Mountains during the LGM (Munroe et al., 2006), plots farthest to the left of any of the Uinta Mountain glaciers in Figure 4, indicating that it required either colder temperatures or greater precipitation than the other glaciers to reach its LGM extent. The Main Fork Provo Glacier plots farther to the right, suggesting that for a given temperature, it did not require as much of an increase in precipitation to advance to its LGM extent. The remaining four glaciers we modeled, including the Main Weber, Bear River, North Fork Duchesne, and Rock Creek Glaciers, would all advance to their maximum LGM extent with a slightly smaller increase in precipitation than had the Main Fork Provo Glacier.

The temperature–precipitation curve for the modeled Main Weber Glacier (Fig. 4) matches the curves for the eastern-most of the modeled glaciers, yet the Main Weber Glacier is toward the western end of the modeling domain. Although end moraines in the Weber Valley are well preserved, pervasive land-sliding may have obscured additional moraines farther downvalley, so it is possible that ice advanced farther than the moraines Oviatt (1994) interpreted as the LGM terminal moraines. In this case, the temperature–precipitation curve for the glacier (Fig. 4) would be translated toward a greater temperature depression. Another possible explanation for the Main Weber Glacier modeling results is that the trend of winter storm tracks during the LGM were somewhat different from today and less precipitation was received in the headwaters of the Weber Valley than in other valleys. Given the highly variable nature of precipitation patterns in mountainous regions, it should not be expected that precipitation patterns during the LGM would necessarily be identical to those observed today. As noted by Laabs et al. (2006), minor differences in winter storm tracks could locally result in non-uniform changes in precipitation patterns. However, ELA reconstructions of paleoglaciers in southwestern Colorado indicate that regional storm tracks across the San Juan Mountains, ~300 km southeast, were not significantly altered during the LGM (Leonard, 1984).

The validity of our assumptions that the temperature depression and vertical temperature gradients during the LGM were uniform across the western end of the Uinta Mountains warrants some additional discussion. Based on model simulations of the effects of Lake Bonneville on regional climate, Hostetler et al. (1994) suggest that the presence of the lake resulted in a regional cooling compared to simulations with no lake. Similar effects due to proglacial lakes south of the Barents–Kara ice sheet in Eurasia have also been modeled (Krinner et al., 2004). However, in the case of Lake Bonneville, the influence of the lake only reduced July temperatures by ca. 0.5 °C in the Wasatch Range and Uinta Mountains (Hostetler et al., 1994). Thus, the magnitude of regional cooling in the model domain due to the presence of Lake Bonneville may have been minor during the ablation season. It is also possible that the difference between modern and LGM vertical temperature gradients across the model domain may not have been uniform. Modern temperature lapse rates are relatively shallow in the western Uintas and Wasatch Mountains, and mean annual precipitation is greater (Laabs et al., 2006). An increase in atmospheric moisture would result in even shallower temperature lapse rates, so if the increase in precipitation across the model domain during the LGM was not uniform, it is possible that LGM temperature lapse rates would not necessarily be similar to modern lapse rates. The overall impact of large lakes on their surrounding climate is to narrow the annual climatic variability; that is, winters are generally warmer and wetter (if the lake is unfrozen) and summers are generally cooler. However, the absolute impact of Lake Bonneville on temperature (including lapse rate) and precipitation, in addition to secondary climate-input parameters such as cloudiness and relative humidity, on adjacent regions remains uncertain until more data are available. Because the modern climatic trends in the area adjacent to Lake Bonneville are similar to the expected impact of a large lake, we can conclude that the climatic deviation required to simulate LGM ice extent in valleys closer to Lake Bonneville is greater than in valleys farther east.

LGM temperature depression

We hesitate to try to identify a single temperature depression value for the LGM in the western Uinta Mountains. Laabs et al. (2006) suggested that an intersection of the temperature–precipitation curves for Lake Fork and Yellowstone Glaciers and could imply a cooling of ~5°C during the LGM. This scenario is reasonable, but our modeling also produced temperature–precipitation curve intersections for the Main Fork Provo and Lake Fork Glaciers, as well as the Little Cottonwood and Swifts Canyon Glaciers, at a temperature depression of ~8.5°C. We use these different intersections to bracket a potential temperature depression range of 5.0 to 8.5°C. In the warmer end of this range, our results suggest that glaciers would have required an increase in precipitation ranging from 2× to greater than 3.5×, with glaciers farther west generally requiring more precipitation to reach their LGM extent. However, independent constraints on either LGM temperature or precipitation are required to make more specific conclusions about the local LGM climate.

https://doi.org/10.1016/j.yqres.2007.10.014 Published online by Cambridge University Press

At the colder end of the 5.0 to 8.5°C range, model simulations suggest that precipitation values during the LGM would have been slightly less than half to slightly above modern values, and glaciers farther west required more precipitation than those to the east. The presumed southerly shift in the jet stream during the LGM, supported by global and regional climate modeling (e.g., Bartlein et al., 1998; Bromwich et al., 2004), would have likely increased precipitation in the northern Great Basin. Lemons et al. (1996) suggest that, based on sediment yield rates in deltas formed in Lake Bonneville, the northern Great Basin received ca. 1.3× enhancement of precipitation during the LGM. Thus, it is unlikely that precipitation in the Uinta Mountains during the LGM would have been much less than modern, so we conclude that LGM temperatures were likely no more than 7°C colder than today. However, based on amino acid paleothermometry, Kaufman (2003) estimated that temperatures in the Lake Bonneville basin during the last full-glacial interval were depressed by 7 to 13°C. The warmer end of this range overlaps the colder end of the temperature range we suggest. Additionally, simulations using a regional climate model coupled to a general circulation model suggest cooling in the western Uintas during the LGM was ca. 8.5°C during July (Hostetler et al., 1994). The colder end of Kaufman's (2003) estimate, as well as the temperature depression suggested by Hostetler et al. (1994), would necessitate that throughout the western Uinta Mountains, half the modern amount of precipitation, at most, was received during the LGM. Based on the results of Lemons et al. (1996) and the global and regional climate modeling results (e.g., Bartlein et al., 1998; Bromwich et al., 2004), we find a scenario with such intense cooling in the Uintas unlikely.

Placing additional constraints on the warmer end of potential LGM cooling in the Uinta Mountains is more problematic. Munroe and Mickelson (2002) reconstructed glacier ELAs for paleoglaciers in the northern Uinta Mountains and inferred a temperature depression of 5.5°C and an increase in precipitation of ~3× during the LGM. Our modeling results suggest that a temperature depression of 5.5°C would be accompanied by a precipitation increase of 2× in the eastern part of the modeling domain and greater than 3.5× in the far western end of the range, so the precipitation estimate of Munroe and Mickelson (2002) is slightly greater than what our results suggest for most of the model domain. Leonard (1989) inferred a temperature depression of 8.5°C during the LGM based on ELA reconstructions for glaciers across the Colorado Rocky Mountains, assuming precipitation during the LGM was similar to modern. Using a combination of degree-day modeling and ELA data from glacier reconstructions, Brugger (2006) estimated LGM temperature depressions in the Sawatch Range of central Colorado of 7.0 to 8.5°C. Therefore, the results of these previous studies are generally consistent with our estimated temperature depression.

Laabs et al. (2006) estimated, based on their modeling results and the results of Kaufman (2003), that temperatures were likely 6 to 7°C colder than modern if the southwestern Uinta Mountains were 1–2× wetter than modern. That our estimate of temperature depression (5 to 7°C) is similar is not surprising, given that we used the same approach to estimating paleoclimatic conditions, though we used climate data and geomorphic data from different basins in the Uintas. Our modeling results do, however, add additional support to the hypothesis that Lake Bonneville amplified precipitation in the western Uinta Mountains.

Conclusions

During the LGM, the western end of the Uinta Mountains was occupied by the Western Uinta Ice Field and a system of distributary glaciers, whereas farther east in the range, glaciers were constrained to individual valleys. Cosmogenic ^{10}Be surface-exposure ages of boulders atop the outermost LGM moraine in the North Fork Provo Valley suggest that ice reached its maximum extent by 17.4±0.5 ka, slightly post-dating the hydrologic maximum of Lake Bonneville. Although these ages are consistent with moraine ages from elsewhere in the Uinta Mountains and Wasatch Range, there are notable differences between the chronology of glacial activity in the Uintas and other ranges throughout the Middle and Southern Rocky Mountains that may reflect the importance of regional-scale climatic controls on ice extent (e.g., Licciardi et al., 2004) or temporal variability in the start of deglaciation. Moraine ages in the western Uintas are generally 1–3 ka younger than moraines in the Wyoming and Colorado Rocky Mountains. Paired ^{26}Al/^{10}Be measurements from Bald Mountain Pass, situated near the former center of the ice field, yield an exposure age of 14.0±0.5 ka. However, due to shielding by snow cover, this age provides only a minimum constraint on the timing of deglaciation of the western part of the range, which likely occurred at least 1000 yr prior to the apparent exposure ages. Thus, the collapse of the Western Uinta Ice Field may have occurred over a period of less than 2–3 ka that was roughly coincident with the climate-driven regression of Lake Bonneville from the Provo shoreline.

We interpret simulations of the Western Uinta Ice Field using the mass/energy-balance and ice-flow model developed by Plummer and Phillips (2003) to suggest that temperatures during the LGM in the western Uinta Mountains were likely 5 to 7°C colder than today with an associated increase in precipitation of 2 to 3.5 times modern values. These results, especially toward the cooler and drier end of this range, are generally consistent with previous estimates of LGM climate in the Uinta Mountains and elsewhere in the region. Although temperature lapse rates may have been variable across the model domain, glaciers in the western-most valleys required significantly more precipitation to reach their reconstructed LGM extent if temperature depression was uniform. As previously suggested by Munroe and Mickelson (2002) and Munroe et al. (2006), enhanced moisture derived from pluvial Lake Bonneville, only 50 km upwind of the westernmost glaciers in the Uinta Mountains, was likely responsible for such a precipitation distribution. Additionally, the cosmogenic surface-exposure ages suggest a general synchroneity between the timing of glacier retreat and the regression of Lake Bonneville. Efforts are currently underway to obtain additional surface-exposure ages from both terminal and recessional moraines elsewhere in the western Uinta Mountains and basal radiocarbon ages from cirque lakes in the Uinta and Wasatch ranges, and further refinement of the Lake Bonneville hydrograph (e.g., Godsey et al., 2005) should

https://doi.org/10.1016/j.yqres.2007.10.014 Published online by Cambridge University Press

help elucidate the climatic relationship between Lake Bonneville and the Uinta Mountains.

Acknowledgments

This research was funded by NSF grant EAR-0345277. Additional support was provided by the Geological Society of America, the Ashley National Forest, the Purdue Rare Isotope Measurement Lab, and the Department of Geology and Geophysics at the University of Wisconsin, Madison. Comments from D. Douglass, V. Rinterknecht, and one anonymous reviewer are greatly appreciated.

Appendix A. Supplementary data

Supplementary data associated with this article can be found, in the online version, at doi:10.1016/j.yqres.2007.10.014.

References

Atwood, W.W., 1909. Glaciation of the Uinta and Wasatch Mountains. U.S. Geological Survey Professional Paper 61. 96 pp.

Bartlein, P.J., Anderson, K.H., Anderson, P.M., Edwards, M.E., Mock, C.J., Thompson, R.S., Webb, R.S., Webb III, T., Whitlock, C., 1998. Paleoclimate simulations for North America over the past 21,000 years: features of the simulated climate and comparisons with paleoenvironmental data. Quaternary Science Reviews 17, 549–585.

Benson, L., Thompson, R.S., 1987. The physical record of lakes in the Great Basin. In: Ruddiman, W.F., Wright Jr., H.E. (Eds.), North American and adjacent oceans during the last deglaciation. Geological Society of America. The Geology of North America, Boulder, CO, K-3, pp. 241–260.

Benson, L., Madole, R., Phillips, W., Landis, G., Thomas, T., Kubik, P., 2004. The probable importance of snow and sediment shielding on cosmogenic ages of north-central Colorado Pinedale and pre-Pinedale moraines. Quaternary Science Reviews 23, 193–206.

Benson, L., Madole, R., Landis, G., Gosse, J., 2005. New data for Late Pleistocene Pinedale alpine glaciation in southwestern Colorado. Quaternary Science Reviews 24, 49–60.

Bierman, P.R., Marsella, K.A., Patterson, C., Davis, P.T., Caffee, M., 1999. Mid-Pleistocene cosmogenic minimum-age limits for pre-Wisconsinan glacial surfaces in southwestern Minnesota and southern Baffin Island: a multiple nuclide approach. Geomorphology 27, 25–39.

Bierman, P.R., Caffee, M.W., Davis, P.T., Marsella, K., Pavich, M., Colgan, P., Mickelson, D., Larsen, J., 2002. Rates and timing of earth surface processes from *in situ*-produced cosmogenic Be-10. In: Grew, E.S. (Ed.), Beryllium — mineralogy, petrology, and geochemistry. Reviews in Mineralogy and Geochemistry, vol. 50, pp. 25–39.

Briner, J.P., Swanson, T.W., 1998. Using inherited cosmogenic Cl to constrain glacial erosion rates at the Cordilleran ice sheet. Geology 26, 3–6.

Bromwich, D.H., Torancinta, E.R., Wei, H., Oglesby, R.J., Fastook, J.L., Hughes, T.J., 2004. Polar MM5 simulations of the winter climate of the Laurentide Ice Sheet at the LGM. Journal of Climate 17, 3415–3433.

Brown, E.T., Edmond, J.M., Raisbeck, G.N., Yiou, F., Kurz, M.D., 1992. Effective attenuation lengths of cosmic rays producing ^{10}Be and ^{26}Al in quartz: implications for surface exposure dating. Geophysical Research Letters 19, 369–372.

Brugger, K.A., 2006. Late Pleistocene climate inferred from the reconstruction of the Taylor River Glacier Complex, southern Sawatch Range, Colorado. Geomorphology 75, 318–329.

Colgan, P.M., Bierman, P.R., Mickelson, D.M., Caffee, M., 1998. Variations in glacial erosion near the southern margin of the Laurentide Ice Sheet, south-central Wisconsin, USA: Implications for cosmogenic dating of glacial terrains. Geological Society of America Bulletin 114, 1581–1591.

Daly, C., Neilson, R.P., Phillips, D.L., 1994. A statistical topographic model for mapping climatological precipitation over mountainous terrain. Journal of Applied Meteorology 33, 140–158.

Diodato, N., 2005. The influence of topography co-variables on the spatial variability of precipitation over small regions of complex terrain. International Journal of Climatology 25, 351–363.

Dunne, J., Elmore, D., Muziker, P., 1999. Scaling factors for the rates of production of cosmogenic nuclides for geometric shading and attenuation at depth on sloped surfaces. Geomorphology 27, 3–11.

Fastook, J., Chapman, J.E., 1989. A map-plane finite-element model: three modeling experiments. Journal of Glaciology 35, 48–52.

Godsey, H.S., Currey, D.R., Chan, M.A., 2005. New evidence for an extended occupation of the Provo shoreline and implications for regional climate change, Pleistocene Lake Bonneville, Utah, USA. Quaternary Research 63, 212–223.

Goovaerts, P., 2000. Geostatistical approaches to incorporating elevation into the spatial interpolation of rainfall. Journal of Hydrology 228, 113–129.

Gosse, J.C., Phillips, F.M., 2001. Terrestrial in situ cosmogenic nuclides: theory and application. Quaternary Science Reviews 20, 1475–1560.

Gosse, J.C., Klein, J., Evenson, E.B., Lawn, B., Middleton, R., 1995. Beryllium-10 dating of the duration and retreat of the last Pinedale glacial sequence. Science 268, 1329–1333.

Hallet, B., Putkonen, J., 1994. Surface dating of dynamic landforms: young boulders on aging moraines. Science 265, 937–940.

Hostetler, S.W., Giorgi, F., Bates, G.T., Bartlein, P.J., 1994. Lake-atmosphere feedbacks associated with paleolakes Bonneville and Lahontan. Science 263, 665–668.

Kaplan, M.R., Ackert Jr., R.P., Singer, B.S., Douglass, D.C., Kurz, M.D., 2004. Cosmogenic nuclide chronology of millennial-scale glacial advances during O-isotope Stage 2 in Patagonia. Geological Society of America Bulletin 116, 308–321.

Kaufman, D.S., 2003. Amino acid paleothermometry of Quaternary ostracodes from the Bonneville Basin, Utah. Quaternary Science Reviews 22, 899–914.

Krinner, G., Mangerud, J., Jakobsson, M., Crucifix, M., Ritz, C., Svendsen, J.I., 2004. Enhanced ice-sheet growth in Eurasia owing to adjacent ice-dammed lakes. Nature 427, 429–432.

Kubik, P.W., Ivy-Ochs, S., Masarik, J., Frank, M., Schlüchter, C., 1998. ^{10}Be and ^{26}Al production rates deduced from an instantaneous even within the dendro-calibration curve, the landslide of Köfels, Ötz Valley, Austria. Earth and Planetary Science Letters 161, 231–241.

Laabs, B.J.C., Carson, E.C., 2005. Glacial geology of the southern Uinta Mountains. In: Dehler, C.M., Pederson, J.L., Sprinkel, D.A., Kowallis, B.J. (Eds.), Uinta Mountain Geology, Publication 33. Utah Geological Association, Salt Lake City, UT, pp. 235–253.

Laabs, B.J.C., Plummer, M.A., Mickelson, D.M., 2006. Climate during the last glacial maximum in the Wasatch and southern Uinta Mountains inferred from glacier modeling. Geomorphology 37, 300–317.

Lal, D., 1991. Cosmic-ray labeling of erosion surfaces: in situ nuclide production rates and erosion models. Earth and Planetary Science Letters 104, 424–439.

Lemons, D.R., Milligan, M.R., Chan, M.A., 1996. Paleoclimatic implications of late Pleistocene sediment yield rates for the Bonneville Basin, northern Utah. Palaeogeography, Palaeoclimatology, Palaeoecology 123, 147–159.

Leonard, E.M., 1984. Late Pleistocene equilibrium-line altitudes and modern snow accumulation patterns, San Juan Mountains, Colorado, U.S.A. Arctic and Alpine Research 16, 65–76.

Leonard, E.M., 1989. Climatic change in the Colorado Rocky Mountains: estimates based on modern climate at late Pleistocene equilibrium-lines. Arctic and Alpine Research 21, 245–255.

Licciardi, J.M., Kurz, M.D., Clark, P.U., Brook, E.J., 1999. Calibration of cosmogenic ^{3}He production rates from Holocene lava flows in Oregon, USA, and effects of the Earth's magnetic field. Earth and Planetary Science Letters 172, 261–271.

Licciardi, J.M., Clark, P.U., Brook, E.J., Pierce, K.L., Kurz, M.D., Elmore, D., Sharma, P., 2001. Cosmogenic 3He and 10Be chronologies of the late Pinedale northern Yellowstone ice cap, Montana, USA. Geology 29, 1095–1098.

Licciardi, J.M., Clark, P.U., Brook, E.J., Elmore, D., Sharma, P., 2004. Variable responses of western U.S. glaciers during the last glaciation. Geology 32, 81–84.

Licciardi, J.M., Pierce, K.L., Kurz, M.D., Finkel, R.C., 2005. Refined chronologies of Yellowstone ice cap and Teton Range outlet glacier fluctuations during the late Pleistocene. Geological Society of America Abstracts with Programs 37, 41.

Lipps, E.W., Marchetti, D.W., Gosse, J.C., 2005. Revised chronology of late Pleistocene glaciers, Wasatch Mountains, Utah. Geological Society of America Abstracts with Programs 37, 41.

Ludwig, K.R., 2003. User's manual for Isoplot 3.00. Berkeley Geochronology Center Special Publications 4.

McCoy, W.D., Williams, L.D., 1985. Applications of an energy-balance model to the late-Pleistocene Little Cottonwood Canyon glacier with implications regarding the paleohydrology of Lake Bonneville. In: Kay, P.A., Diaz, H.F. (Eds.), Problems of and prospects for predicting Great Salt Lake levels, pp. 40–53.

Mitchell, V.L., 1976. The regionalization of climate in the western United States. Journal of Applied Meteorology 15, 920–927.

Munroe, J.S., 2005. Glacial geology of the northern Uinta Mountains. In: Dehler, C.M., Pederson, J.L., Sprinkel, D.A., Kowallis, B.J. (Eds.), Uinta Mountain Geology, Publication 33. Utah Geological Association, Salt Lake City, UT, pp. 215–234.

Munroe, J.S., Mickelson, D.M., 2002. Last Glacial Maximum equilibrium-line altitudes and paleoclimate, northern Uinta Mountains, Utah, U.S.A. Journal of Glaciology 48, 257–266.

Munroe, J.S., Laabs, B.J.C., Shakun, J.D., Singer, B.S., Mickelson, D.M., Refsnider, K.A., Caffee, M.W., 2006. Latest Pleistocene advance of alpine glaciers in the southwestern Uinta Mountains, northeastern Utah, USA: evidence for the influence of local moisture sources. Geology 34, 841–844.

Muzikar, P., Elmore, D., Granger, D.E., 2003. Accelerator mass spectrometry in geologic research. Geological Society of America Bulletin 114, 643–654.

Oerlemans, J., Knap, W.H., 1998. A 1 year record of global radiation and albedo in the ablation zone of Morteratschgletscher, Switzerland. Journal of Glaciology 44, 231–238.

Oerlemans, J., Anderson, B., Hubbard, A., Huybrechts, P., Johannesson, T., Knap, W.H., Schmeits, M., Stroeven, A.P., van de Wal, R.S.W., Wallinga, J., Zuo, Z., 1998. Modelling the response of glaciers to climate warming. Climate Dynamics 15, 267–274.

Owen, L.A., Finkel, R.C., Minnich, R.A., Perez, A.E., 2003. Extreme southwestern margin of late Quaternary glaciation in North America: timing and controls. Geology 31, 729–732.

Oviatt, C.G., 1994. Quaternary geologic map of the upper Weber River drainage basin, Summit County, Utah. Utah Geological Survey Map 156.

Oviatt, C.G., 1997. Lake Bonneville fluctuations and global climate change. Geology 25, 155–158.

Paterson, W.S.B., 1994. The physics of glaciers, third edition. Elsevier, Oxford.

Phillips, F.M., Zreda, M.G., Gosse, J.C., Klein, J., Evenson, E.B., Hall, R.D., Chadwick, O.A., Sharma, P., 1997. Cosmogenic ^{36}Cl and ^{10}Be ages of Quaternary glacial and fluvial deposits of the Wind River Range, Wyoming. Geological Society of America Bulletin 109, 1453–1463.

Plummer, M.A., 2002. Paleoclimate conditions during the last deglaciation inferred from combined analysis of pluvial and glacial records: [Unpublished Ph.D. dissertation], New Mexico Institute of Mining and Technology, Socorro, New Mexico, 346 pp.

Plummer, M.A., Phillips, F.M., 2003. A 2-D numerical model of snow/ice energy balance and ice flow for paleoclimatic interpretation of glacial geomorphic features. Quaternary Science Reviews 22, 1389–1406.

Putkonen, J., Swanson, T., 2003. Accuracy of cosmogenic ages for moraines. Quaternary Research 59, 255–261.

Refsnider, K.A., 2006. Late Pleistocene glacial and climate history of the Provo River drainage, Uinta Mountains, Utah. [Unpublished M.S. thesis]: University of Wisconsin - Madison, Madison, WI, 121.

Refsnider, K.A., Laabs, B.J.C., Mickelson, D.M., 2007. Glacial geology and equilibrium line altitude reconstructions for the Provo River drainage, Uinta Mountains, Utah, U.S.A. Arctic, Antarctic, and Alpine Research. Arctic, Antarctic, and Alpine Research 39, 529–536.

Stone, J.O., 2000. Air pressure and cosmogenic isotope production. Journal of Geophysical Research 105, 23,753–23,759.

Stuiver, M., Reimer, P.J., Reimer, R.W., 2005. *CALIB 5.0.2* [WWW program and documentation]. University of Washington and Belfast, Queen's University of Belfast. URL: <www.calib.org>.

Zreda, M.G., Phillips, F.M., Elmore, D., 1994. Cosmogenic ^{36}Cl in unstable landforms 2. Simulations and measurements on eroding moraines. Water Resources Research 30, 3127–3136.